

Repository Istituzionale dei Prodotti della Ricerca del Politecnico di Bari

Rationalizing the Molecular Design of Hole-Selective Contacts to Improve Charge Extraction in Perovskite Solar Cells

This is a post print of the following article

Original Citation:
Rationalizing the Molecular Design of Hole-Selective Contacts to Improve Charge Extraction in Perovskite Solar Cells / Wang, Q., Mosconi, E., Wolff, C., Li, J., Neher, D., De Angelis, F., Suranna, G.P., Grisorio, R., Abate, A.. - In: ADVANCED ENERGY MATERIALS. - ISSN 1614-6832. - STAMPA. - 9:28(2019). [10.1002/aenm.201900990]

Availability:
This version is available at http://hdl.handle.net/11589/176029 since: 2021-03-11

Published version
DOI:10.1002/aenm.201900990

Publisher:

Terms of use:

(Article begins on next page)

26 November 2026

Rationalizing the Molecular Design of Hole-Selective Contacts to Improve Charge Extraction in Perovskite Solar Cells

Qiong Wang,[1] Edoardo Mosconi,[2] Christian Wolff,[3] Junming Li,[1] Dieter Neher,[3] Filippo De Angelis,[2,4,5] Gian Paolo Suranna,[6,7] Roberto Grisorio,[6,7]* Antonio Abate[1,8,9]*

[1]Helmholtz-Zentrum Berlin für Materialien und Energie, Kekuléstraße 5, 12489 Berlin, Germany

[2]Computational Laboratory for Hybrid/Organic Photovoltaic (CLHYO), Istituto CNR di Scienze e Tecnologie Molecolari (ISTM-CNR), Via Elce di Sotto 8, 06123 Perugia, Italy

[3]Institute for Physics and Astronomy, University of Potsdam, Karl-Liebknecht-Straße 24−25, 14476 Potsdam-Golm, Germany

[4]D3-CompuNet, Istituto Italiano di Tecnologia, Via Morego 30, 16163 Genova, Italy.

[5]Department of Chemistry, Biology and Biotechnology, University of Perugia, Via Elce di Sotto 8, 06123, Perugia, Italy.

[6]Dipartimento di Ingegneria Civile, Ambientale, del Territorio, Edile e di Chimica (DICATECh), Politecnico di Bari, Via Orabona 4, 70125 Bari, Italy

[7]CNR-NANOTEC, Istituto di Nanotecnologia, c/o Campus Ecotekne, Università del Salento, Via Monteroni, 73100 Lecce, Italy

[8]Department of Chemical, Materials and Production Engineering, University of Naples Federioco II, Piazzale Tecchio 80, 80125 Fuorigrotta, Naples, Italy.

[9]State Key Laboratory of Photocatalysis on Energy and Environment, Institute of Advanced Energy Materials, Fuzhou University, Fuzhou, Fujian 350002, China

RG roberto.grisorio@poliba.it; AA antonio.abate@helmholtz-berlin.de; antonio.abate@unina.it

Abstract
Two new hole selective materials (HSMs) based on dangling methylsulfanyl groups connected to the C-9 position of the fluorene core are synthesised and applied in perovskite solar cells. Being structurally similar to a half of Spiro-OMeTAD molecule, these HSMs (referred as **FS** and **DFS**) share similar redox potentials but are endowed with slightly higher hole mobility, due to the planarity and large extension of their structure. Competitive power conversion efficiency (up to 18.6%) is achieved by using the new HSMs in suitable perovskite solar cells. Time-resolved photoluminescence decay measurements and electrochemical impedance spectroscopy show more efficient charge extraction at the HSM/perovskite interface with respect to Spiro-OMeTAD, which is reflected in higher photocurrents exhibited by **DFS**/**FS**-integrated perovskite solar cells. Density functional theory simulations reveal that the interactions of methylammonium with methylsulfanyl groups in **DFS**/**FS** strengthen their electrostatic attraction with the perovskite surface, providing an additional path for hole extraction compared to the sole presence of methoxy groups in Spiro-OMeTAD. Importantly, the low-cost synthesis of **FS** makes it significantly attractive for the future commercialisation of perovskite solar cells.

Keywords
hole selective materials, sulphur, hole extraction, triple-cation perovskite, perovskite solar cells

Introduction

Lead halide perovskites present some outstanding photo-physical properties as well as structural flexibility.[1] Perovskite solar cells (PSCs) in particular have shown great potential as the alternative, highly efficient photovoltaics (PVs) to the well-established PV technology.[2] The solution-processed perovskite films show a low density of bulk trap states,[3] which enriches the possible architectures of PSCs.[4-6] Moreover, monolithic films can be easily formed between the electron selective contact (ESC) and the hole selective contact (HSC).[6, 7] This further benefits the charge transport inside the bulk perovskite film.[8, 9] To further promote the power conversion efficiency (PCE) of PSCs, researchers emphasise the optimisation of the interface between perovskite film and ESC/HSC.[10] Tan *et al*.[11] modified the TiO_2 compact layer with chlorine and they found that the Cl-doped TiO_2 can form stronger Pb-Cl binding at the surface of perovskite film, as predicted by theory,[12] which delivered an improved PSCs photovoltaic performance and stability. Meanwhile, more works are conducted on the optimisation of the perovskite/HSC interface, because there are more rooms to play with the organic hole selective materials (HSMs) compared to the limited options with the inorganic electron selective counterparts.[13] Therefore, new HSMs have been reported with the main effort to replace the most commonly used but expensive 2,2′,7,7′-tetrakis(N,N-di-*p*-methoxyphenylamine)-9,9′-spirobifluorene (Spiro-OMeTAD).[14] Another important section of the fundamental research around the HSM optimisation moves towards the improvement of the device stability.[15] For example, Joong Joen *et al*.[16] synthesised a fluorene-terminated HSM with a fine-tuned energy level and a high glass transition temperature, which resulted in a high efficiency of 23.2% with robust thermal stability.

At the nanometric level, the passivation of the perovskite film under the assistance of Lewis bases could play a crucial role in the charge transfer dynamics at the perovskite/HSM interface.[17] In particular, electron donating thiophene groups bind to the lead ions (Pb^{2+}) coordinatively showed excellent defect passivation effect of perovskite film and resulted in enhanced PCE in devices.[18] Later, Saliba *et al*.[19] reported the synthesis of (2'7'-bis(bis(4-methoxyphenyl)amino)spiro[cyclopenta[2,1-b:3,4-b']dithiophene-4,9'-fluorene] (commonly known as **FDT**) that contains two thiophene groups as the π-linker one of the Spiro-OMeTAD fluorenes. They observed a slightly higher efficiency in devices using **FDT** than their control cells using Spiro-OMeTAD, which was explained by the interaction between the thiophene group in **FDT** and perovskite film. Other studies suggested that the presence of thiophene[20] or phenothiazine[21] is beneficial for the charge extraction due to the potential trap passivation *via* Pb–S interactions. In another work, Hu *et al*.[22] introduced three new spirofluorene-based

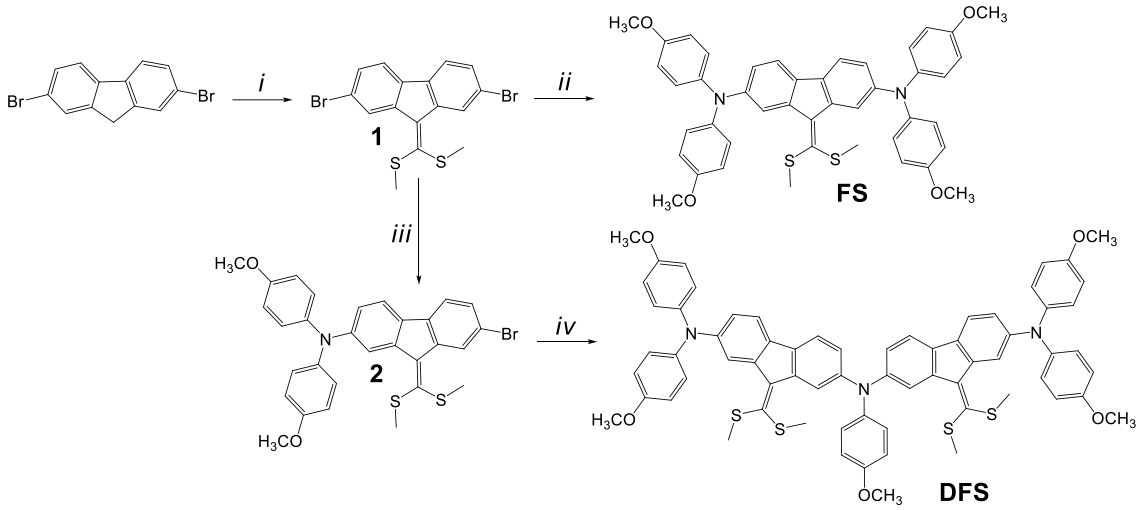
HSMs by replacing the para-methoxy substituent in Spiro-OMeTAD with methylsulfanyl, N,N-dimethylamino and ethyl groups. They found that the methylsulfanyl substituted spirofluorene gave a higher efficiency than the other two HSMs, also outperforming Spiro-OMeTAD. Time-resolved photoluminescence (PL) measurements showed that such compound had a better hole extraction compared to Spiro-OMeTAD. However, the reason behind the enhanced hole extraction efficiency was not further investigated.

Here, we designed two new HSMs with the aim to connect the methylsulfanyl groups with the C-9 position of the fluorene scaffold characterising the Spiro-OMeTAD reference. The advantage of these two materials (denoted as **DFS** and **FS**) over those previously reported[22] is that the highest occupied molecular orbital (HOMO) and the lowest unoccupied molecular orbital (LUMO) energies of these two materials resemble those of Spiro-OMeTAD. Employing molecules with matched energy levels may elucidate additional interactions and exclude the influence on the photovoltaic performance of PSCs brought by the energy alignment differences in HSMs. We carried out time-resolved photoluminescence and electrochemical impedance measurements to quantify the hole extraction efficiency by our HSMs. Supported by density functional theory (DFT) calculations, we attribute the enhanced hole extraction at the perovskite interface to the additive electrostatic attraction between the methylsulfanyl groups of **DFS**/**FS** and surface methylammonium of the perovskite film, thus creating a new pathway for charge transfer. In perspective, this study paves the way for new concepts in the molecular design of novel HSMs.

Results and Discussion

Synthesis and characterisation

The synthetic sequences for the obtainment of **FS** and **DFS** are reported in **Scheme 1**. The sulphur-containing fluorene-based core of these HSMs was obtained straightforwardly from commercially available 2,7-dibromofluorene. The synthetic details, nuclear magnetic resonance (NMR) spectra as well as cost estimate[23] are reported in the Supporting Information. (**Schemes S1-S4** and **Figures S1-S4**)



Scheme 1. Synthetic sequence for the obtainment of **FS** and **DFS**: i) *tert*-BuONa, CS_2, methyl iodide, DMSO (95% yield); *ii*) *p*-methoxy-diphenylamine, $Pd_2(dba)_3/{}^tBu_3P$, *tert*-BuONa, toluene, 100 °C (81% yield); *iii*) *p*-methoxy-diphenylamine, $Pd(AcO)_2$/dppf, *tert*-BuONa, toluene, 100 °C (34% yield); *iv*) *p*-anisidine, $Pd_2(dba)_3/{}^tBu_3P$, *tert*-BuONa, toluene, 100 °C (65% yield).

The stability and thermal behaviour of **FS** and **DFS** were evaluated by thermogravimetric analysis (TGA) and differential scanning calorimetry (DSC) measurements in comparison with the thermal properties of Spiro-OMeTAD reference. (**Figure S5a** and **5b**) Both in the case of **FS** and **DFS**, the 5% weight loss of the sample commonly accepted as the event associated with the material decomposition, was observed at 347 °C, indicating satisfactory thermal stability, although lower than that of Spiro-OMeTAD (424 °C). The relatively lower decomposition and glass transition temperatures exhibited by **FS** and **DFS** are due to the peculiar functionalization of fluorene C-9 position, which is traditionally considered as the weakness point of the aromatic structure and introduces dangling groups endowed with higher degrees of ro-vibrational freedom.[24] The normalised UV/Vis absorption spectra of **FS** and **DFS** in CH_2Cl_2 are shown in **Figure S5c**. It shows that the two absorption profiles are very similar with an absorption maximum at 380 nm and a shoulder at longer wavelengths. The absorption maximum recorded

for Spiro-OMeTAD in the same experimental conditions was observed at 386 nm. The optical band gap of **FS** and **DFS** determined from the absorption onset (417 nm and 426 nm for **FS** and **DFS**, respectively) are consistent with the different conjugation extension of the two molecules. The main difference in the optical properties concerning that of Spiro-OMeTAD concerns the presence of a broad and weak absorption feature in the wavelength ranging from 450 nm to 600 nm. According to our previous work,[25] this absorption feature can be ascribed to the sulphur atoms involved n→π* transition. To further clarify this aspect, we theoretically investigated the absorption spectra and the electronic properties of **FS** and **DFS** and compared them with those of Spiro-OMeTAD. As it can be deduced from inspection of **Table 1**, the absorption maxima calculated by Time-Dependent DFT (TDDFT) are in good agreement with the experimental measurements.

Table 1. Measured UV-vis absorption maxima (CH_2Cl_2) along with the calculated values of the strongest transitions calculated by Time-Dependent DFT.

	Abs. Max. (nm)	
	Exp.	Calc.
Spiro-OMeTAD	386	387
FS	380	379
DFS	380	397

The calculated UV-vis absorption spectra in comparison with the experimental data are given in **Figure 1a**. Based on calculations, we assign the weak absorption band above 500 nm for **FS** to the HOMO→LUMO transition (**Figure 1b)**, involving the -S-CH_3 groups as final states. The main signal at around 380 nm is related to the HOMO→LUMO+1 transition, mainly involving the molecular core, and higher-lying transition at 365 nm is associated to excitation within the fluorene–S-CH_3 groups (**Figure 1b)**. Similar behaviour is found for **DFS** where the low-intensity signal is found at 508 nm. The oxidation potentials of **FS** and **DFS** were determined by cyclic voltammograms (CVs) (**Figure S5d)**. By the electrochemical data, the HOMOs of **FS** and **DFS** are estimated to be –5.05 eV and –5.06 eV, respectively. Meanwhile, Spiro-OMeTAD exhibits a value of –5.09 eV as calculated from **Figure S5d**. We also calculated the oxidation potential by DFT calculations, which resulted in the values of -5.11 eV, -4.92 eV and -4.98 eV, for **FS**, **DFS** and Spiro-OMeTAD, respectively, in line with the electrochemical measurements. The energy levels of **FS**, **DFS** and Spiro-OMeTAD are aligned with ESMs and perovskite layer in **Figure 2a**, which shows the high similarity in energy levels of the studied HSMs in this work. Hole mobility of pristine **FS** and **DFS** are characterised using space-charge-limited current (SCLC) method with details given in the supporting information (**Figure S6**). Pristine **DFS** and

FS show hole mobility of 2.5 × 10^{-4} cm^2/Vs and 2.1× 10^{-4} cm^2/Vs, slightly higher than that of pristine Spiro-OMeTAD (1.3 × 10^{-4} cm^2/Vs)[26].

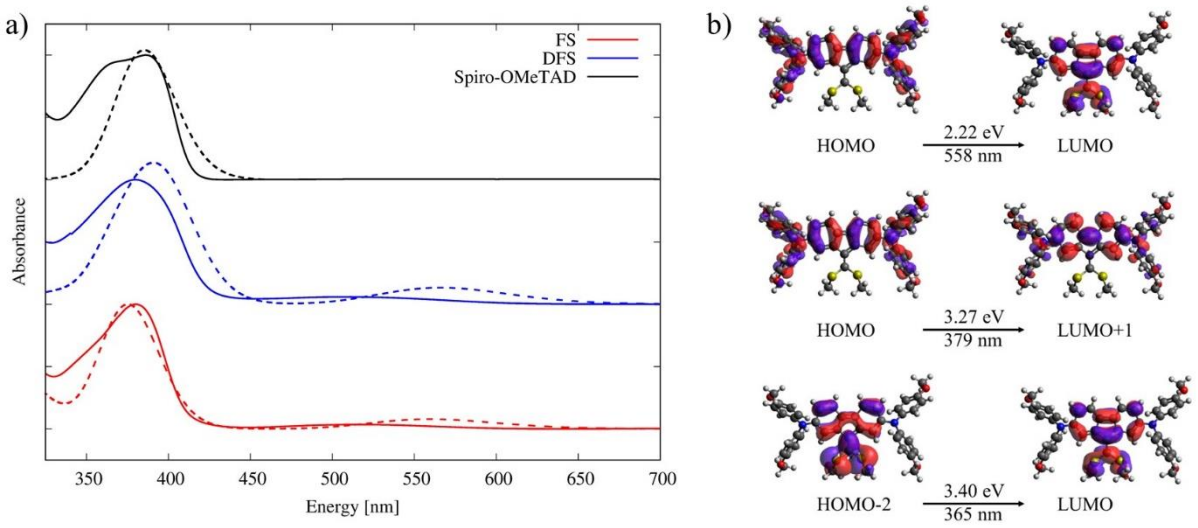


Figure 1. a) Absorption spectra for **FS** (red), **DFS** (blue) and Spiro-OMeTAD (black). The experimental data are given with solid lines while the calculated spectra are reported with dashed lines. b) Electronic transitions calculated by TDDFT for the **FS** molecule.

Device Characterization

DFS and **FS** have been applied in PSCs where planar SnO_2 deposited from chemical bath deposition[27] is used as the electron selective contact, and $Cs_{0.05}(FA_{0.87}MA_{0.13})_{0.95}Pb(I_{0.87}Br_{0.13})_3$ triple cation perovskite[8] is used as the light absorber. The cross-sectional Scanning Electron Microscopy (SEM) images of the devices are given in **Figure S7**. It shows that a monolithic perovskite film is deposited between the SnO_2 ESM and the HSM. The similar perovskite film thickness of around 550 nm is observed for all devices. The light current-voltage (*JV*) curve of the champion devices is given in **Figure 2b**. It shows that devices using **DFS** and **FS** as HSMs can achieve efficiencies of 18.4% and 18.6%, respectively, which is competitive to that of the standard, highly optimised, Spiro-OMeTAD (19.0%). The external quantum efficiency (EQE) spectra were measured, as given in **Figure S8**. The integrated short-circuit current density (J_{sc}) from EQE measurement matches well with the value measured from the *JV* scan. Dark *JV* given in **Figure S9** shows a better suppression of dark current for devices using **DFS** and **FS** as HSMs than that of Spiro-OMeTAD. The box charts of photovoltaic parameters of 18 devices are given in **Figure S10**. Particularly, we notice that there is a general enhancement in photocurrent for devices with **DFS**/**FS** compared to those of Spiro-OMeTAD based devices, on a par with the champion *JV* curves given in **Figure 2**. To gain a better understanding of the interaction between **DFS**/**FS** and perovskite at the interface,

we conducted steady state and time-resolved PL (TRPL) spectroscopy measurement and the electrochemical impedance spectroscopy measurement.

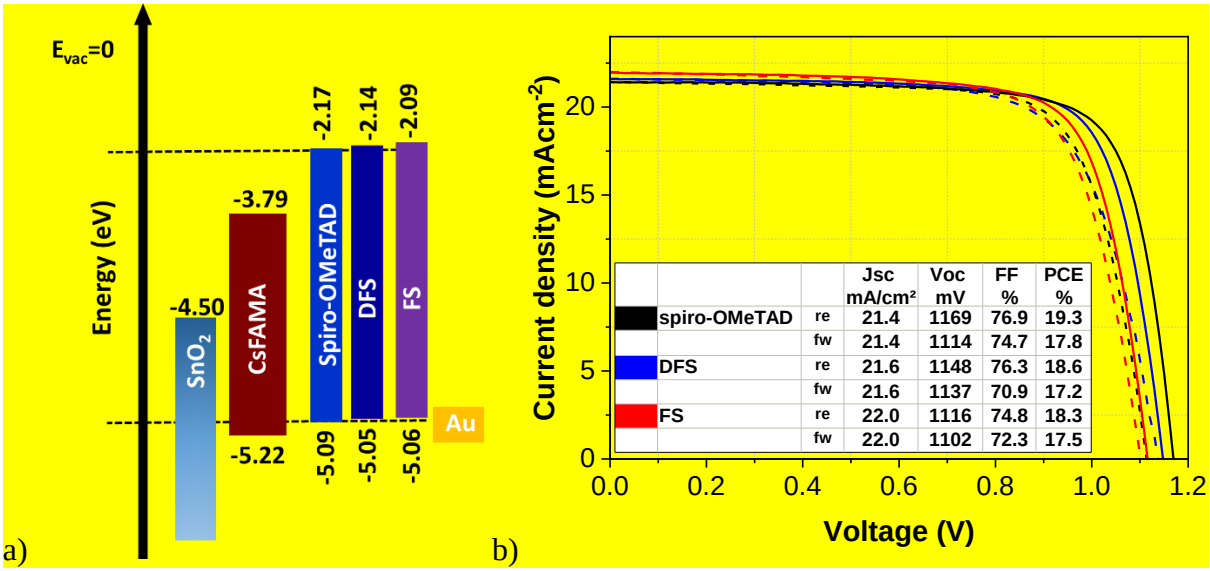


Figure 2. a) Scheme of energy level alignment for each component of PSCs. Note: the energy level of SnO_2, CsFAMA, and Au were extracted from the literature data.[28] b) Photovoltaic characterisation of **DFS** (blue line) and **FS** (red line) in comparison with Spiro-OMeTAD (black line) as the control. Measured under 1 Sun (AM 1.5G, 100 mW/cm^2) illumination. Scan rate: 100 mV/s. Reverse scan (referred as "re" in the inset table): scanning from high potential to low potential (solid line). Forward scan (referred as "fw" in the inset table): scanning from low potential to high potential (dash line). The inset table summarises the photovoltaic parameters.

The TRPL spectroscopy measurement of perovskite films with and without ESMs/HSMs have been the subject of several studies[29]mainly conducted by Stranks *et al*.[29-31] as well as others.[32] Following absorption of a photon, an electron and hole pair is generated. Charge carriers can either recombine radiatively or be trapped by defects in the bulk and at the surface of the sample. Most of these trap states are shallow in lead-halide perovskites, which means the captured electrons and holes can be released in a short time scale in the range of nanoseconds.[3, 4] This explains the long electron-hole lifetime in perovskite film.[33] Radiative recombination happens in a very short time, and normally appears as a power-law decay in the TRPL measurement, whereas the non-radiative recombination by monomolecular shows a monoexponential decay in the TRPL measurement.[30] It should be noted that the actual TRPL data of the same perovskite sample is highly influenced by the pulse fluence.[30]

When the perovskite film is deposited adjacent to an ESM or HSM, the interpretation of TRPL data can be more complicated. First, electrons or holes can be extracted by the ESM or HSM and then lead to a decrease in PL intensity. The more efficient in charge extraction, the more efficient in quenching of PL intensity. Secondly, the ESM/HSM may bring some defects at the

interface with the perovskite, which results in non-radiative recombination and leading to drops in PL intensity. The second role played by ESM/HSM has been confirmed by Stolterfoht *et al.*[34] who compared a range of ESMs and HSMs using the TRPL and absolute PL spectra measurement. However, it should be noted that these two roles played by ESMs/HSMs both involve a monomolecular process that leads to a monoexponential decay in PL intensity. Moreover, these two processes happen simultaneously and are connected. As a result, when we fit the TRPL curve with a monoexponential curve, the PL lifetime calculated from the fitting contains the charge transfer process as well as the non-radiative recombination process. The reciprocal of the PL lifetime refers to the overall rate constant of these two processes. A faster charge transfer process or increased non-radiative recombination will both lead to a shorter PL lifetime.

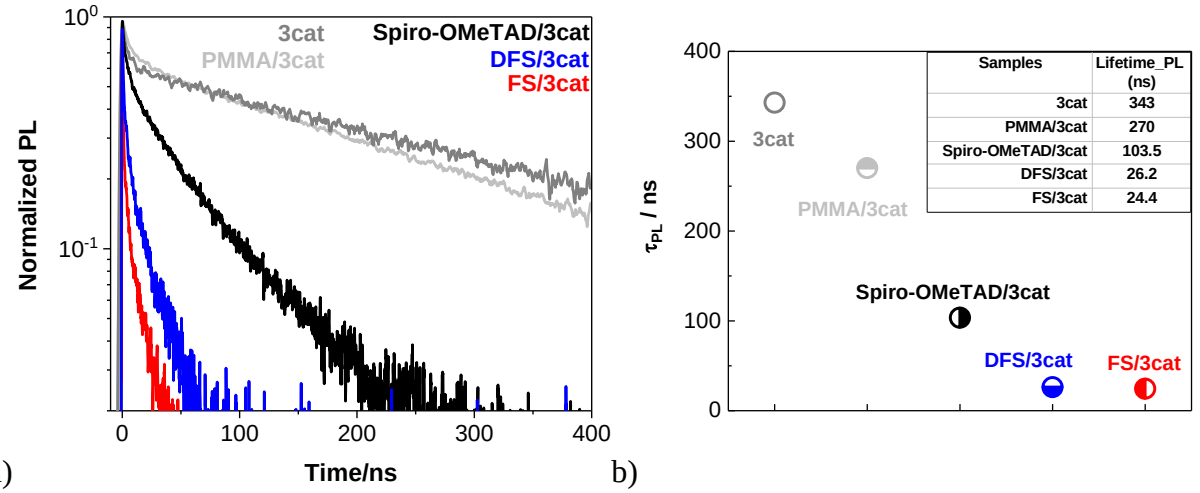


Figure 3. a) Time-resolved photoluminescence decay of pristine perovskite film (grey line), perovskite film covered by poly(methyl methacrylate) (PMMA) (light grey line), Spiro-OMeTAD (black line), **DFS** (blue line) and **FS** (red line). b) PL lifetime (τ_{PL}) calculated by monoexponential fitting of the linear part of the PL decay curve given in a): pristine perovskite film (grey circle), perovskite film covered by PMMA (light grey half-filled circle), Spiro-OMeTAD (black half-filled circle), **DFS** (blue half-filled circle) and **FS** (red half-filled circle). Note: "3cat" stands for the triple-cation perovskite used in this work.

Figure 3a shows the PL decay of perovskite film with and without top layers. We can observe a faster decrease in the PL intensity of the three HSMs compared to pristine perovskite film. In particular, the PL decay of perovskite films coated with either **DFS** or **FS**, lead to a stronger quenching effect of the PL intensity compared to Spiro-OMeTAD. Steady-state PL spectra were given in **Figure S11**. It shows a clear decrease in the absolute PL intensity in samples: neat perovskite > Spiro-OMeTAD > DFS > FS, which agrees well with what is observed in TRPL

measurement. Based on the previous work,[30-32] we fit the PL decay curve with the monoexponential decay function given in **Eq.1**.[34, 35]

$$I_t = I_0 \exp(-\frac{t}{\tau}) \qquad \textbf{Eq.1}$$

where I_t and I_0 refer to the PL intensity at time t and zero, and τ is the PL lifetime. It measures the decay rate of PL intensity. For perovskite films without any ESMs/HSMs, τ is the reciprocal of the rate constant of non-radiative recombination process. For perovskite films coated with ESMs/HSMs, τ takes into account the rate constant of charge transfer and non-radiative recombination. **Figure 3b** shows the PL lifetime, τ_{PL} of perovskite films with and without HSMs. The pristine perovskite films show a slightly longer lifetime than that of perovskite films coated by a thin layer of poly(methyl methacrylate) (PMMA), which indicates the robustness of triple cation perovskite films during the TRPL measurement conducted in ambient atmosphere. **DFS** and **FS** as HSMs show a similar value of 26.2 ns and 24.4 ns, respectively, which is about one quarter of that of Spiro-OMeTAD (103.5 ns). As previously discussed, the short PL lifetime indicates a faster charge transfer process or a faster non-radiative recombination process. To investigate which process dominates we conducted electrochemical impedance spectroscopy measurements.

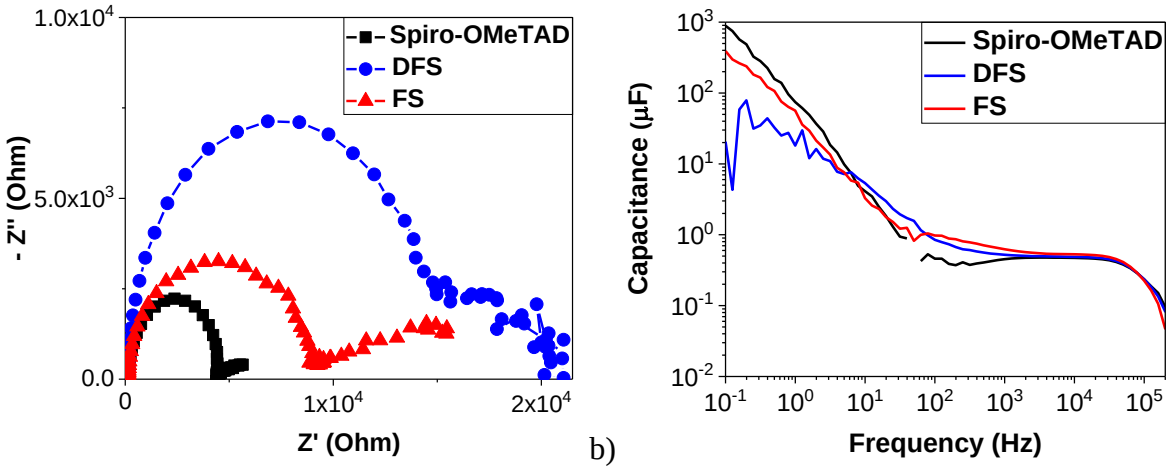


Figure 4. a) Nyquist plot and b) calculated capacitance of devices based on Spiro-OMeTAD (black), **DFS** (blue) and **FS** (red), respectively, measured at open-circuit under the illumination of 550 nm LED with a light intensity equivalent to 0.1 Sun.

Impedance spectra of the devices were conducted at open-circuit at a low light intensity equivalent to 0.1 Sun to study the recombination information inside the system. **Figure 4a** shows the Nyquist plot of the devices. Based on Bisquert and Garcia-Belmonte's work,[36] the first semi-circle appeared at high frequency range at 10^3~10^5 Hz correlates to the dielectric

property of bulk perovskite film, and the second semi-circle presented at low-frequency range at 10^0~10^1 Hz correlates to the surface charge recombination at the interface of perovskite and electron/hole selective contact layers. Meanwhile, the diameter of the semicircle correlates to the transport resistance of perovskite film and recombination resistance at the interface for the first semi-circle and the second semi-circle, respectively. The frequency where the imaginary part of impedance, -Z'' reaches the maximum can be referred to as the maximum frequency, f_{max}. The reciprocal of f_{max} correlates to a time constant.[37] In particular, $(f_{max})^{-1}$ of the second semi-circle corresponds to the recombination lifetime. To distinguish this recombination lifetime from the non-radiative recombination lifetime extracted from TRPL measurement, it is noted as τ_2. It should be noted that the recombination lifetime extracted from impedance spectra contain different meanings from the non-radiative recombination lifetime and they were measured under different conditions. One would expect, $\tau_2 > \tau_{PL}$. It can be seen from **Figure 4a** that the diameter of the first semi-circle and the second semi-circle in devices of **DFS** is larger than that of **FS** and the latter is larger than that of Spiro-OMeTAD. As we discussed above, the diameter of the second semi-circle refers to the recombination resistance at the interface of perovskite and ESC/HSC. As a result, we can conclude that that the recombination resistance in **DFS**–based devices is larger than that of **FS** and larger than that of Spiro-OMeTAD. This information further correlates to the capacitance or charge carrier density at the interface. **Figure 4b** shows the dependence of capacitance as a function of frequency. It can be seen that the chemical capacitance at low frequency of the devices of **DFS** is lower than that of **FS** and lower than that of Spiro-OMeTAD. In other words, the charge carrier density at the interface for devices of **DFS** is less than that of **FS** and less than that of Spiro-OMeTAD. It means that at the same quantity of photo-generated electron and holes in the bulk of perovskite film, devices with **DFS** and **FS** is more efficient in charge extraction and thus less charges are accumulated at the interface.[37, 38] This conclusion supports that the shorter PL lifetime observed in TRPL measurement is attributed to the faster charge transfer. In addition, it is also noted that the bulk capacitance at high frequency range is identically the same for these devices because the bulk capacitance is mainly related to the film thickness and area of the bulk perovskite film. As we explained in the experimental section in the supporting information, the devices were prepared under the same condition. Also, the film thickness of the perovskite layer can be measured from the cross-sectional SEM image given in **Figure S7**.

Meanwhile, we also notice that there is a general tread in the V_{oc}: Spiro-OMeTAD > DFS > FS. It would be quite interesting to study the origin for the difference in V_{oc} of these HSMs. Indeed, V_{oc} of a PSC can be influenced by many factors, such as bulk non-radiative recombination

inside the perovskite film and the interfacial non-radiative recombination at the interface between perovskite and HSMs. As we used the same device architecture for all the HSMs in this work, one would expect the bulk recombination in the perovskite film to be the same. From the TRPL measurement, the impedance spectroscopy and the dark current measurement, we believe that interfacial recombination for **FS** and **DFS** was more suppressed than that of Spiro-OMeTAD. One possible reason for the relative low V_{oc} in **FS** and **DFS** based regular structured PSCs can be the migration of gold from the metal electrode.[39] **Figure S7** shows that **FS** and **DFS** have a slightly low film thickness compared to Spiro-OMeTAD. This is resulted from the relatively low molecular weight of **FS** and **DFS** that are deposited at the same concentration and spin-coating speed as that of Spiro-OMeTAD. A thinner film thickness of HSM is not beneficial for n-i-p devices because the gold migration undermines the potential V_{oc}, which is what we have observed for **FS** and **DFS** based PSCs. The relatively high J_{sc} but low V_{oc} together with comparable *FF* in **FS** and **DFS** based PSCs finally make them of similar photovoltaic performance to Spiro-OMeTAD based devices.

Comparing the molecular structure of **FS** with that of Spiro-OMeTAD, it is clear how, let alone the spiro-structure, the main difference resides in the presence of a methylsulfanyl group at the fluorene C-9 position. In a simulation study on surface interaction between methoxy anchors and lead iodide perovskite by Torres *et al.*[40], they reported that the methoxy group adsorbed to the surface of perovskite *via* the interaction with methylammonium cation governed by electrostatic interaction. To further investigate the interface interaction between **DFS**/**FS** and perovskite, we conducted the DFT simulations. In particular, we modelled the interface of the more stable MAI-terminated perovskite slab exposing (001) facet with **FS** and Spiro-OMeTAD. Notice that this is an idealised surface, since we use a fully passivated MAI-terminated surface, while disorder and surface reconstruction may alter the exact nature of the interface. Still, by performing a direct comparison between the HSMs interacting with the same perovskite surface, we may extract useful information on the fundamental interactions ruling the functioning of such interface. The optimised geometries and the electronic properties of the two HSM/perovskite interfaces are shown in **Figure 5**. As suggested by Torres et al.[40], Spiro-OMeTAD interacts *via* hydrogen bonding methoxy oxygen with the MA^+ cations of the perovskite surface, as highlighted by the blue circle in **Figure 5c**. In the **FS** HSM case, we found that in addition to the MA^+---O-CH_3 hydrogen bond (highlighted by the blue circle in **Figure 5a**), a stabilising interaction was formed between the sulfur atoms and the surface MA^+ cations (highlighted by the red circle in **Figure 5a**). We then calculated the energy (ΔE) associated with the interface formation. We found that the **FS** molecule has a strongly favoured

interaction energy (ΔE = -1.52 eV) compared to that of Spiro-OMeTAD (ΔE = -0.11 eV). This underlines that the additional specific hydrogen bond interaction between MA^+ and methylsulfanyl group in **FS** significantly increases the stability of the perovskite/**FS** interface. The electronic properties of the perovskite/HSM interface presented in terms of the interface density of states (DOS) are given in **Figure 5b** and **5d**. **FS** shows more positive HOMO energy concerning Spiro-OMeTAD when interacting with the MAI-terminated perovskite slab. This more positive energy level of the **FS** HSM and the related energy alignment at the perovskite valence band leads to the higher driving force for the hole extraction, and thus a faster charge transfer as observed in the TRPL and the impedance measurements. The overall picture extracted from the theoretical simulation suggest that (i) the electrostatic effect between the methylsulfanyl and MA^+ brings about an extra interaction path for **DFS**/**FS** compared to the methoxy group bound with MA^+ in the case of Spiro-OMeTAD; and (ii) the electronic properties and relative energy alignment at the valence band between the **FS** and perovskite provides a higher driving force for the hole injection process upon photoexcitation.

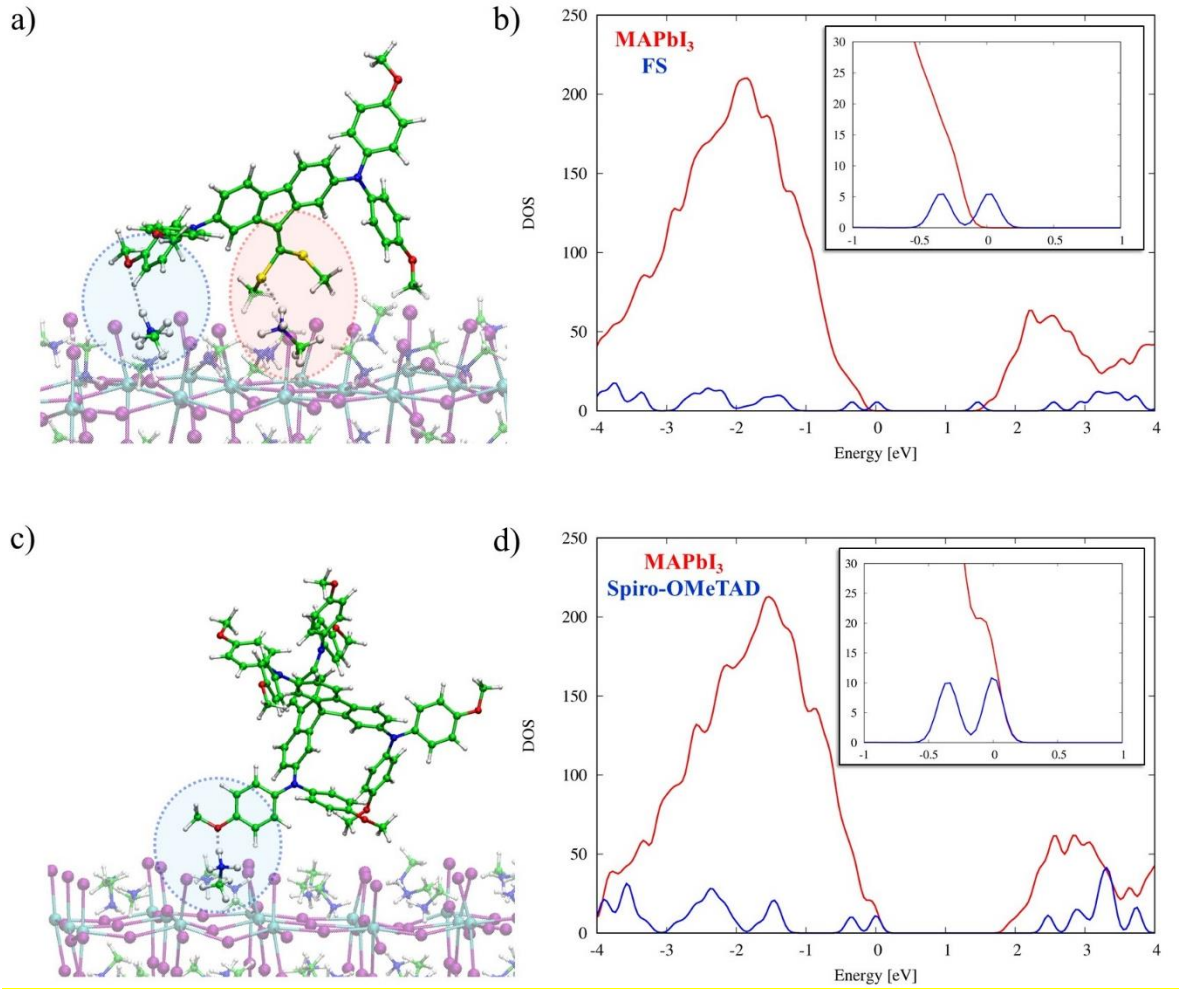


Figure 5. Optimised geometries of the a) **FS**@$MAPbI_3$ and c) Spiro-OMeTAD@$MAPbI_3$ exposing the MAI-terminated surface. DOS for the b) **FS**@$MAPbI_3$ interface and d) Spiro-

OMeTAD@$MAPbI_3$. We set at zero the energy of the HOMO for both systems that are associated with the HOMO of the **FS** molecule.

Conclusions

In this work, we reported two new HSMs (**DFS** and **FS**) that exhibit similar LUMO and HOMO positions to that of Spiro-OMeTAD. The TRPL measurement together with impedance spectra revealed a more efficient hole extraction in **DFS** and **FS** than that of Spiro-OMeTAD. DFT calculations revealed that the fast charge extraction was originated from i) the formation of an additional path for charge extraction, *i.e.* the electrostatic effect between methylsulfanyl in **FS**/**DFS** and MA^+ at perovskite surface, compared to the hydrogen bond between methoxy group and MA^+, and ii) the preferred energy alignment at the interface of **FS**/**DFS** and perovskite. As a result, this work reveals the reasons for the better charge transfer for **FS**/**DFS** that contain a methylsulfanyl group. More importantly, these findings pave the way to innovative ideas regarding the molecular design of the next generation of HSMs for application in efficient perovskite solar cells.

Supporting information

Synthesis and characterisation of **DFS** and **FS**, preparation and fabrication of perovskite solar cells, cross-sectional SEM images of devices, dark JV, box chart of photovoltaic parameters, and so on can be found in the supporting information.

Acknowledgement

R.G. and G.P.S. acknowledge the Bridge-Early Stage COMPOSTRONICS project (cod. 5730587, Austrian Research Promotion Agency-FFG) for funding. A.A. acknowledges the financial support from the National Natural Science Foundation of China (project no. 21750110442).

Reference

[1] M. Saliba, J.-P. Correa-Baena, M. Grätzel, A. Hagfeldt, A. Abate, Angewandte Chemie International Edition 2018, 57, 2554; Q. Lin, A. Armin, R. C. R. Nagiri, P. L. Burn, P. Meredith, Nature Photonics 2014, 9, 106; M. Anaya, J. F. Galisteo-López, M. E. Calvo, J. P. Espinós, H. Míguez, The Journal of Physical Chemistry Letters 2018, 9, 3891; T. Jesper Jacobsson, J.-P. Correa-Baena, M. Pazoki, M. Saliba, K. Schenk, M. Grätzel, A. Hagfeldt, Energy & Environmental Science 2016, 9, 1706.

[2] Q. Wang, N. Phung, D. Di Girolamo, P. Vivo, A. Abate, Energy & Environmental Science 2019; Y. Rong, Y. Hu, A. Mei, H. Tan, M. I. Saidaminov, S. I. Seok, M. D. McGehee, E. H. Sargent, H. Han, Science 2018, 361, eaat8235.

[3] D. Meggiolaro, F. De Angelis, ACS Energy Letters 2018, 3, 2206.

[4] D. Meggiolaro, S. G. Motti, E. Mosconi, A. J. Barker, J. Ball, C. Andrea Riccardo Perini, F. Deschler, A. Petrozza, F. De Angelis, Energy & Environmental Science 2018, 11, 702.

[5] G. Landi, H. C. Neitzert, C. Barone, C. Mauro, F. Lang, S. Albrecht, B. Rech, S. Pagano, Advanced Science 2017, 4, 1700183.

[6] M. Saliba, J.-P. Correa-Baena, C. M. Wolff, M. Stolterfoht, N. Phung, S. Albrecht, D. Neher, A. Abate, Chemistry of Materials 2018, 30, 4193.

[7] S.-H. Turren-Cruz, A. Hagfeldt, M. Saliba, Science 2018, eaat3583.

[8] M. Saliba, T. Matsui, J.-Y. Seo, K. Domanski, J.-P. Correa-Baena, M. K. Nazeeruddin, S. M. Zakeeruddin, W. Tress, A. Abate, A. Hagfeldt, M. Grätzel, Energy & Environmental Science 2016, 9, 1989.

[9] M. Saliba, T. Matsui, K. Domanski, J.-Y. Seo, A. Ummadisingu, S. M. Zakeeruddin, J.-P. Correa-Baena, W. R. Tress, A. Abate, A. Hagfeldt, M. Grätzel, Science 2016, aah5557; J.-P. Correa-Baena, L. Nienhaus, R. C. Kurchin, S. S. Shin, S. Wieghold, N. T. Putri Hartono, M. Layurova, N. D. Klein, J. R. Poindexter, A. Polizzotti, S. Sun, M. G. Bawendi, T. Buonassisi, Chemistry of Materials 2018, 30, 3734.

[10] S.-H. Turren-Cruz, M. Saliba, M. T. Mayer, H. Juárez-Santiesteban, X. Mathew, L. Nienhaus, W. Tress, M. P. Erodici, M.-J. Sher, M. G. Bawendi, M. Grätzel, A. Abate, A. Hagfeldt, J.-P. Correa-Baena, Energy & Environmental Science 2018, 11, 78; J.-P. Correa-Baena, W. Tress, K. Domanski, E. H. Anaraki, S.-H. Turren-Cruz, B. Roose, P. P. Boix, M. Grätzel, M. Saliba, A. Abate, A. Hagfeldt, Energy & Environmental Science 2017, 10, 1207.

[11] H. Tan, A. Jain, O. Voznyy, X. Lan, F. P. García de Arquer, J. Z. Fan, R. Quintero-Bermudez, M. Yuan, B. Zhang, Y. Zhao, F. Fan, P. Li, L. N. Quan, Y. Zhao, Z.-H. Lu, Z. Yang, S. Hoogland, E. H. Sargent, Science 2017.

[12] E. Mosconi, E. Ronca, F. De Angelis, The Journal of Physical Chemistry Letters 2014, 5, 2619.

[13] J. Liu, Y. Wu, C. Qin, X. Yang, T. Yasuda, A. Islam, K. Zhang, W. Peng, W. Chen, L. Han, Energy & Environmental Science 2014, 7, 2963; X.-D. Zhu, X.-J. Ma, Y.-K. Wang, Y. Li, C.-H. Gao, Z.-K. Wang, Z.-Q. Jiang, L.-S. Liao, Advanced Functional Materials 2019, 29, 1807094; Y.-K. Wang, Z.-C. Yuan, G.-Z. Shi, Y.-X. Li, Q. Li, F. Hui, B.-Q. Sun, Z.-Q. Jiang, L.-S. Liao, Advanced Functional Materials 2016, 26, 1375.

[14] S. Paek, P. Qin, Y. Lee, K. T. Cho, P. Gao, G. Grancini, E. Oveisi, P. Gratia, K. Rakstys, S. A. Al-Muhtaseb, C. Ludwig, J. Ko, M. K. Nazeeruddin, Advanced Materials 2017, 29, 1606555; H. D. Pham, T. T. Do, J. Kim, C. Charbonneau, S. Manzhos, K. Feron, W. C. Tsoi, J. R. Durrant, S. M. Jain, P. Sonar, Advanced Energy Materials 2018, 8, 1703007; B. Xu, Z. Zhu, J. Zhang, H. Liu, C.-C. Chueh, X. Li, A. K.-Y. Jen, Advanced Energy Materials 2017, 7, 1700683.

[15] F. Wang, Y. Cao, C. Chen, Q. Chen, X. Wu, X. Li, T. Qin, W. Huang, Advanced Functional Materials 2018, 28, 1803753; F. Liu, Q. Li, Z. Li, Asian Journal of Organic Chemistry 2018, 7, 2182; A. Abate, S. Paek, F. Giordano, J.-P. Correa-Baena, M. Saliba, P. Gao, T. Matsui, J. Ko, S. M. Zakeeruddin, K. H. Dahmen, A. Hagfeldt, M. Gratzel, M. K. Nazeeruddin, Energy & Environmental Science 2015, 8, 2946.

[16] N. J. Jeon, H. Na, E. H. Jung, T.-Y. Yang, Y. G. Lee, G. Kim, H.-W. Shin, S. Il Seok, J. Lee, J. Seo, Nature Energy 2018, 3, 682.

[17] J.-W. Lee, H.-S. Kim, N.-G. Park, Accounts of Chemical Research 2016, 49, 311; D. P. Nenon, K. Pressler, J. Kang, B. A. Koscher, J. H. Olshansky, W. T. Osowiecki, M. A. Koc, L.-W. Wang, A. P. Alivisatos, Journal of the American Chemical Society 2018, 140, 17760; R. Grisorio, M. E. Di Clemente, E. Fanizza, I. Allegretta, D. Altamura, M. Striccoli, R. Terzano, C. Giannini, M. Irimia-Vladu, G. P. Suranna, Nanoscale 2019, 11, 986.

[18] N. K. Noel, A. Abate, S. D. Stranks, E. S. Parrott, V. M. Burlakov, A. Goriely, H. J. Snaith, ACS Nano 2014, 8, 9815.
[19] M. Saliba, S. Orlandi, T. Matsui, S. Aghazada, M. Cavazzini, J.-P. Correa-Baena, P. Gao, R. Scopelliti, E. Mosconi, K.-H. Dahmen, F. De Angelis, A. Abate, A. Hagfeldt, G. Pozzi, M. Graetzel, M. K. Nazeeruddin, Nature Energy 2016, 1, 15017.
[20] Q.-Q. Ge, J.-Y. Shao, J. Ding, L.-Y. Deng, W.-K. Zhou, Y.-X. Chen, J.-Y. Ma, L.-J. Wan, J. Yao, J.-S. Hu, Y.-W. Zhong, Angewandte Chemie International Edition 2018, 57, 10959.
[21] R. Grisorio, B. Roose, S. Colella, A. Listorti, G. P. Suranna, A. Abate, ACS Energy Letters 2017, 2, 1029.
[22] Z. Hu, W. Fu, L. Yan, J. Miao, H. Yu, Y. He, O. Goto, H. Meng, H. Chen, W. Huang, Chemical Science 2016, 7, 5007.
[23] R. Grisorio, L. De Marco, C. Baldisserri, F. Martina, M. Serantoni, G. Gigli, G. P. Suranna, ACS Sustainable Chemistry & Engineering 2015, 3, 770.
[24] R. Grisorio, G. Allegretta, P. Mastrorilli, G. P. Suranna, Macromolecules 2011, 44, 7977.
[25] R. Grisorio, C. Piliego, M. Striccoli, P. Cosma, P. Fini, G. Gigli, P. Mastrorilli, G. P. Suranna, C. F. Nobile, The Journal of Physical Chemistry C 2008, 112, 20076.
[26] M. Li, Z.-K. Wang, Y.-G. Yang, Y. Hu, S.-L. Feng, J.-M. Wang, X.-Y. Gao, L.-S. Liao, Advanced Energy Materials 2016, 6, 1601156; D. Poplavskyy, J. Nelson, Journal of Applied Physics 2003, 93, 341.
[27] E. H. Anaraki, A. Kermanpur, L. Steier, K. Domanski, T. Matsui, W. Tress, M. Saliba, A. Abate, M. Gratzel, A. Hagfeldt, J.-P. Correa-Baena, Energy & Environmental Science 2016, 9, 3128.
[28] M. Ye, C. He, J. Iocozzia, X. Liu, X. Cui, X. Meng, M. Rager, X. Hong, X. Liu, Z. Lin, Journal of Physics D: Applied Physics 2017, 50, 373002; M. Salado, R. K. Kokal, L. Calio, S. Kazim, M. Deepa, S. Ahmad, Physical Chemistry Chemical Physics 2017, 19, 22905.
[29] A. Paulke, S. D. Stranks, J. Kniepert, J. Kurpiers, C. M. Wolff, N. Schön, H. J. Snaith, T. J. K. Brenner, D. Neher, Applied Physics Letters 2016, 108, 113505.
[30] S. D. Stranks, V. M. Burlakov, T. Leijtens, J. M. Ball, A. Goriely, H. J. Snaith, Physical Review Applied 2014, 2, 034007.
[31] E. M. Hutter, G. E. Eperon, S. D. Stranks, T. J. Savenije, The Journal of Physical Chemistry Letters 2015, 6, 3082.
[32] M. B. Johnston, L. M. Herz, Accounts of Chemical Research 2016, 49, 146; J. M. Richter, M. Abdi-Jalebi, A. Sadhanala, M. Tabachnyk, J. P. H. Rivett, L. M. Pazos-Outón, K. C. Gödel, M. Price, F. Deschler, R. H. Friend, Nature Communications 2016, 7, 13941; R. Saxena, A. Kumar, N. Jain, N. K. Kumawat, K. L. Narasimhan, D. Kabra, The Journal of Physical Chemistry C 2018, 122, 1119; C. Wehrenfennig, G. E. Eperon, M. B. Johnston, H. J. Snaith, L. M. Herz, Advanced Materials 2014, 26, 1584; Y. Yamada, T. Nakamura, M. Endo, A. Wakamiya, Y. Kanemitsu, Journal of the American Chemical Society 2014, 136, 11610.
[33] T. Chen, W.-L. Chen, B. J. Foley, J. Lee, J. P. C. Ruff, J. Y. P. Ko, C. M. Brown, L. W. Harriger, D. Zhang, C. Park, M. Yoon, Y.-M. Chang, J. J. Choi, S.-H. Lee, Proceedings of the National Academy of Sciences 2017, 114, 7519; Y. Bi, E. M. Hutter, Y. Fang, Q. Dong, J. Huang, T. J. Savenije, The Journal of Physical Chemistry Letters 2016, 7, 923.
[34] M. Stolterfoht, C. M. Wolff, J. A. Márquez, S. Zhang, C. J. Hages, D. Rothhardt, S. Albrecht, P. L. Burn, P. Meredith, T. Unold, D. Neher, Nature Energy 2018, 3, 847.
[35] C. M. Wolff, F. Zu, A. Paulke, L. P. Toro, N. Koch, D. Neher, Advanced Materials 2017, 29, 1700159.
[36] A. Guerrero, G. Garcia-Belmonte, I. Mora-Sero, J. Bisquert, Y. S. Kang, T. J. Jacobsson, J.-P. Correa-Baena, A. Hagfeldt, The Journal of Physical Chemistry C 2016, 120, 8023; I. Zarazua, J. Bisquert, G. Garcia-Belmonte, The Journal of Physical Chemistry Letters 2016, 7, 525; I. Zarazua, G. Han, P. P. Boix, S. Mhaisalkar, F. Fabregat-Santiago, I. Mora-Seró, J. Bisquert, G. Garcia-Belmonte, The Journal of Physical Chemistry Letters 2016, 7, 5105.
[37] Q. Wang, The Journal of Physical Chemistry C 2018, 122, 4822.
[38] Q. Wang, Physical Chemistry Chemical Physics 2018, 20, 10114.
[39] K. Domanski, J.-P. Correa-Baena, N. Mine, M. K. Nazeeruddin, A. Abate, M. Saliba, W. Tress, A. Hagfeldt, M. Grätzel, ACS Nano 2016, 10, 6306.

[40] A. Torres, L. G. C. Rego, The Journal of Physical Chemistry C 2014, 118, 26947.